International Journal of Heat and Mass Transfer 269 (2026) 129055

Contents lists available at ScienceDirect

International Journal of Heat and Mass Transfer

journal homepage: www.elsevier.com/locate/hmt

Thermal conductivity, emissivity, and solidus and liquidus temperatures of additively manufactured 316L stainless steel (316L SS) using steady-state laser heating-based thermography techniques

Jessica Reyes [a,*], Hunter B. Schonfeld [a], Jeffrey L. Braun [b], Saman Zare [a], Bryan N. Baines [b], John T. Gaskins [b], Michael A. Gallegos [c], David Saiz [c], Bryan Kaehr [c], Patrick E. Hopkins [a,b,d,e]

[a] Department of Mechanical and Aerospace Engineering, University of Virginia, Charlottesville, 22903, VA, USA
[b] Laser Thermal, Charlottesville, 22902, VA, USA
[c] Sandia National Laboratories, Albuquerque, 87123, NM, USA
[d] Department of Materials Science and Engineering, University of Virginia, Charlottesville, 22903, VA, USA
[e] Department of Physics, University of Virginia, Charlottesville, 22903, VA, USA

ARTICLE INFO

Keywords:
Thermal conductivity
Infrared thermography
Solidus
Liquidus
Emissivity

ABSTRACT

Additive manufacturing (AM) can produce materials with complex geometries and lightweight structures, but unlike conventional processes, it can introduce defects such as porosity and phase inhomogeneity that can degrade thermal behavior and lead to unpredictable heating across applications. Because a material's thermal properties are highly sensitive to defects and microstructure, measurements of thermal conductivity, emissivity, and melting temperature provide a powerful, non-contact metrology method to evaluate the quality of AM materials. In this study, we employ laser-based diagnostics on a series of AM 316L stainless-steel samples, measuring thermal conductivity, emissivity, and solidus/liquidus temperatures. Thermal conductivity is calculated by two different steady-state methods: a commercial Thermo-Optical Plane Source (TOPS; Laser Thermal) and a new technique introduced in this work, Steady-State Laser-Induced Thermographic Radiometry (SSLITHER). Our results indicate that the effective thermal conductivity in AM parts decreases by 20%–50%, depending on the printing settings, largely driven by the changes in the relative densities of the samples and by defects introduced during the printing process. We found that low-density samples exhibit lower performance at high temperatures, showing depressed solidus and liquidus temperatures and altered emissivity caused by oxygen content trapped within lack of fusion regions, which modifies surface radiative properties. After laser-induced melting and resolidification (which increases density and forces oxygen out), the effective thermal conductivity and melting temperatures increase, and emissivity is restored. Our work presents the potential for laser-based thermal conductivity, emissivity, and melting temperature measurements as tools for evaluating and improving the performance of AM materials.

1. Introduction

Additive Manufacturing (AM), the process of building materials and structures layer by layer, has gained popularity in recent years due to its ability to create complex geometries, lightweight structures, and reduce material waste, thus enabling rapid production [1]. This innovative technology has become essential in industries such as aerospace and electronics, where design freedom, reduced weight, and cost-effective production are highly valued.

Although AM is demonstrating potential as a game-changer for many technologies and applications, it also carries its drawbacks. Fabrication parameters such as laser power (P), scan speed (v), hatch spacing (h), and powder layer thickness (t) play a critical role in determining the final density of additively manufactured parts [2]. These parameters define the volumetric energy density ($E_d = P/vht$) applied during printing, which directly affects the material's final density [3]. However, despite careful parameter optimization, AM processes remain prone to manufacturing defects, including high porosity, cracks, and lack of fusion (LOF) regions. These defects can significantly affect

* Corresponding author.
E-mail addresses: ymf6cf@virginia.edu (J. Reyes), phopkins@virginia.edu (P.E. Hopkins).

https://doi.org/10.1016/j.ijheatmasstransfer.2026.129055
Received 22 January 2026; Received in revised form 5 May 2026; Accepted 20 May 2026
Available online 3 June 2026

the performance and reliability of the additively manufactured parts. For example, the mechanical properties of AM materials have been extensively studied in direct comparison with cast components [4–7], where parts produced by selective laser melting (SLM) typically exhibit lower fracture strain [4] and shorter fatigue lifetimes [6], primarily driven by differences in defects and microstructure.

In contrast, fewer studies have focused on the thermal properties of additively manufactured materials. These properties are critical in applications where thermal management and stability under extreme conditions are essential, such as aircraft heat exchangers for air conditioning radiators [1], engine oil coolers [8], aircraft engine components for high-temperature combustion chambers [9], and nuclear fuel cladding [10]. In particular, thermal conductivity (κ) of additively manufactured materials is crucial for understanding and optimizing material performance in such demanding environments.

The thermal conductivity of materials is influenced by the material's defects and microstructure, which, on the nanoscopic level, leads to increased thermal carrier (electrons and phonons) scattering events that reduce the efficacy of heat transfer [11–14]. Common defects in AM parts, such as porosity [15–17] and lack of fusion (LOF) [18,19], reduce the thermal conductivity of the proximate region, leading to heat localization and temperature gradients, and concomitant thermo-mechanical failure. Thus, accurate measurements of the thermal conductivity and other thermal properties that are related to thermal carrier scattering rate changes are critical to mitigate these aforementioned thermal challenges.

Further, as the thermal conductivity of materials is directly related to defect concentrations, several prior works have demonstrated that the thermal conductivity of materials can be used as a surrogate probe to qualitatively detect changes in defect density that otherwise are only detectable with more invasive, destructive, or obfuscative methods [13,20–23]. These works highlight the potential for thermal property measurements as a metric of quality control assessments to detect micro-defects in AM components [24].

Previous research has measured the thermal conductivity of precursor AM powders and parts using contact-based measurement techniques [25–27]. These methods, however, have poor spatial resolution and are unable to capture microstructural variations. Moreover, the presence of contact resistance can introduce significant errors [28], particularly when measuring samples with rough surfaces [29]. Thus, non-contact thermal conductivity methods offer immense potential for accurately evaluating AM materials by alleviating these aforementioned limitations of contact-based techniques.

For example, pump–probe thermoreflectance techniques, such as time-domain, frequency-domain and steady-state thermoreflectance (TDTR [30], FDTR [31], and SSTR [32], respectively) are all based on the same principle, where the temperature changes on a sample surface induced from a pump laser are measured as a change in the probe laser reflectivity. In the most common implementations of TDTR, FDTR and SSTR, the focused laser spot sizes are on the order of tens of μm, and thus the measurement's "voxel" is on the order of this spot size in any areal or depth dimension. Thus, while these relatively localized volumes can provide invaluable information about surface-localized changes in the thermal properties, as reported by Simmons et al. [24], these near-surface thermal properties are not necessarily representative of the averaged thermal transport properties in the bulk of the material. While Laser Flash Analysis (LFA) offers a measurement of the average thermal diffusivity through the entire depth of the AM part; this makes LFA incapable of detecting local variations in thermal conductivity caused by micro-structural heterogeneity. Additionally, this method relies on separately measured heat capacity, which can introduce error in the final thermal conductivity [33].

In this work, we demonstrate the use of two different infrared thermography (IRT) approaches operating under steady-state thermal gradient conditions to directly measure the thermal conductivity of AM 316L stainless steel (i.e., these steady state conditions permit a thermal conductivity measurement without *a priori* knowledge of the material's specific heat or density), while also providing thermal measurement volumes with voxel dimensions of hundreds of micrometers up to several millimeters. Most IRT-based techniques applied to AM materials and processes focus on measuring temperature distributions during printing, analyzing thermal gradients that cause microstructure formation (>100 μm), and observing the melting and re-solidification processes in layer-by-layer fabrication [34–38]. However, these studies primarily examine large surface areas, lacking the precision necessary to detect micro-defects.

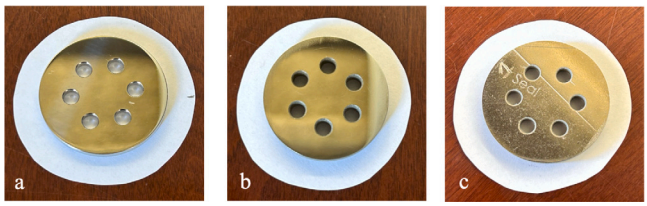

Fig. 1. Samples: (a) 316L-M, (b) 316L-AM-HD, (c) 316L-AM-LD1, built with settings described in Table 1.

The first technique we employ in this work, Steady-State Laser-Induced Thermographic Radiometry (SSLITHER), which is a derivative of our recently developed Steady-State Temperature Differential Radiometry (SSTDR) [39], offers a more localized heating spot and higher resolution (on the order of 100's of micrometers), bridging the gap in spatial resolution between thermoreflectance techniques that operate on the micrometer scale and more traditional IRT and LFA approaches that operate at the millimeter scale. We then turn to our recently developed Thermo-Optical Plane Source (TOPS) technique using a commercialized TOPS instrument from Laser Thermal (LT) [40].

Laser Thermal's TOPS system operates with measurement voxel volumes on the order of millimeters, thus offering comparative sampling volumes as traditional IRT and LFA techniques. However, TOPS operates under steady-state conditions during continuous wave laser heating, similar to SSLITHER, thus providing a direct measurement of thermal conductivity. The agreement between our SSLITHER and TOPS measurements demonstrates promise for these steady-state thermometry methods as tools to measure the thermal conductivity of AM materials and evaluate the post-manufacturing quality of AM parts. Because the AM samples contain porosity, and lack of fusion defects, the values reported here should be interpreted as effective thermal conductivity, κ_{eff}, rather than the intrinsic thermal conductivity of fully dense 316L stainless steel.

To supplement our SSLITHER and TOPS thermal conductivity measurements, we measured the spectral emissivity of the 316L SS samples at room temperature (from 2−5 μm) and at high temperature at the liquidus temperature (from 0.5−1.0 μm). This allows us to evaluate the solidus and liquidus temperatures of 316L SS, demonstrating that the AM part with more defects exhibits a lower solidus and liquidus than higher quality AM and machined 316L SS, which correlates with our thermal conductivity measurements in that the lower density AM part has a reduced effective thermal conductivity and melting temperature.

After melting the lower quality AM part, subsequent measurements of thermal conductivity, solidus, and liquidus temperatures increase to those of the higher quality AM. This indicates the potential for local non-contact thermal conductivity measurements to identify low-quality regions in AM parts and subsequent laser heating to repair and increase the quality of these identified regions.

2. Samples

Samples of 316L stainless steel were prepared using different fabrication methods and parameter sets. Pictures of the samples are shown in Fig. 1. The samples are classified as 316L-M (316L Stainless Steel,

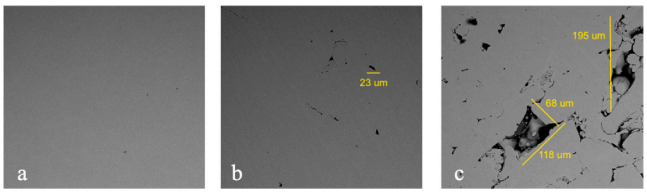

Fig. 2. SEM: (a) 316L-M, (b) 316L-AM-HD, (c) 316L-AM-LD1. Low density samples experience large defect areas (~100 μm) in comparison with high density samples (~20 μm).

Table 1
Processing parameters for high- and low-density samples.

Parameter	Description	High density	Low density
P	Power (W)	113	80
v	Velocity (mm s^{-1})	1400	1727
h	Hatch (μm)	50	50
t	Layer thickness (μm)	30	30

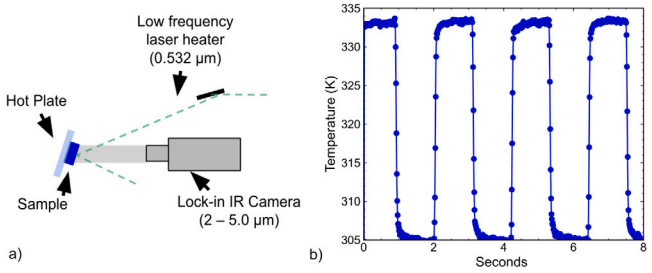

Fig. 3. (a) Schematic of SSLITHER experiment. A low-frequency modulated green laser periodically heats the sample. The resulting surface temperature response is recorded by a lock-in infrared camera (2–5 μm). (b) Sample surface temperature versus time measured by the IR camera. The periodic heating and cooling cycles are synchronized to the laser modulation. (For interpretation of the references to color in this figure legend, the reader is referred to the web version of this article.)

Machined), 316L-AM-HD (316L Stainless Steel, Additive Manufactured, High Density), and 316L-AM-LD (316L Stainless Steel, Additive Manufactured, Low Density); note, three different 316L-AM-LD samples were fabricated under identical conditions, which we denote as 316L-AM-LD-1, -2, and -3. The 316L-AM-HD sample was fabricated using the parameter set shown in Table 1, which employed higher laser power and slower scan speeds. This combination resulted in better melting and uniform solidification, producing higher density samples. In contrast, the 316L-AM-LD samples were fabricated using higher scan speeds and lower energy inputs (Table 1) under the high density tab. These conditions led to incomplete melting areas and higher porosity. All samples are 400 mm diameter and 5 mm thickness.

Scanning Electron Microscopy (SEM) images of 316L-AM-HD and 316L-AM-LD-1, compared to a bulk machined reference, are presented in Fig. 2. These micrographs highlight the differences in microstructure and porosity between the parameter sets, where the high density AM sample exhibits relatively smaller pores (~15 μm, Fig. 2b) as compared to the lower density AM sample, which shows larger pores, cracks, and lack of fusion (LOF) regions that range from 15 to 150 μm.

3. Methodology

3.1. Thermal conductivity measurements with SSLITHER

A schematic of the Steady-State Laser-Induced THErmographic Radiometry (SSLITHER) technique built in this work is shown in Fig. 3. SSLITHER operates by inducing a steady-state temperature gradient via

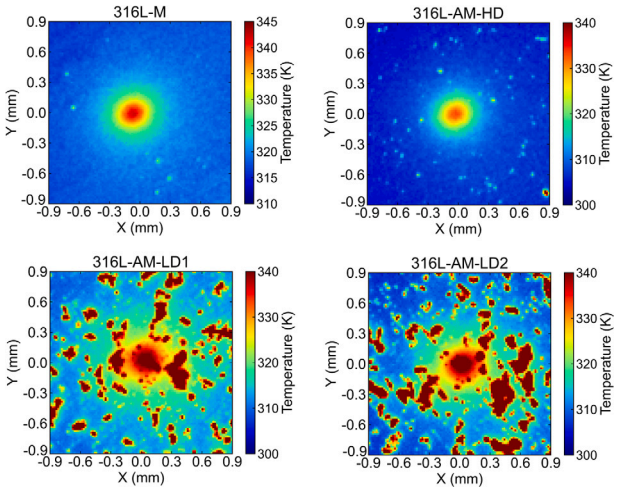

Fig. 4. Steady state temperature profiles of machined, high density AM and low density AM samples measured by infrared thermography under continuous laser heating. The high temperature of the porous layer in 316L-AM-LD1 and 316-AM-LD2 comes from the hot plate; this does not affect our measurements as the laser spot does not cover those areas.

laser heating the sample surface and measuring the radial temperature profile of the sample on the same side as the laser heating event. Thus, the key experimental parameters in an SSLITHER experiment are the laser power and measurement of radial surface temperature. We employ a green laser with a wavelength of 532 nm. The IR camera used in this study (Infratec ImageIR 8380) has a spectral range of 2.5 to 5.5 μm and provides a spatial resolution of 15 μm per pixel. The laser was modulated at low frequency, and lock-in acquisition of the IR camera signal was used to isolate the laser temperature rise from the background and camera noise. The resulting temperature field reaches a stable periodic response, as shown in 3b. We used two different spot sizes, 300 μm and 700 μm; both spot sizes gave the same effective thermal conductivity, a resolution of 15 μm per pixel corresponds to approximately 20 and 47 pixels across the beam diameter, respectively, which provides sufficient spatial sampling of the heated region and surrounding radial profile. Laser power was 0.55 W to ensure the temperature rise was detectable by the IR camera while remaining low enough that the laser only slightly perturbs the sample temperature, so the thermal conductivity can be assumed constant within the imposed temperature gradient.

The IR camera has a minimum temperature detection of −10 °C, for a blackbody like surface (emissivity of unity). In our experiments, stainless steel has a much lower emissivity (0.18–0.22 in the camera wavelength range) and therefore emits less infrared radiation than a blackbody at the same temperature [41]. To obtain temperature readings, the samples were heated on a laboratory hot plate with closed-loop temperature control set at 70 °C. However, the samples reach a temperature around 40 °C, this difference is attributed to thermal contact resistance between the sample and the hot plate, heat loss to the surroundings, and the low emissivity of stainless steel. Thus, the SSLITHER-measured the effective thermal conductivity reported here corresponds to a sample temperature of about 40 °C.

Spatially resolved temperature maps of the samples show how heat propagation can vary in the differing AM manufactured materials, as shown in Fig. 4. In denser samples, heat spreads more uniformly, while in porous samples, the heat flow varies due to the presence of defects and irregularities within the material.

To accurately determine the true temperature from the IR camera, we performed infrared variable angle spectroscopic ellipsometry (IR-VASE Mark II, J.A. Woollam) to measure the infrared emissivity. We used IR-VASE to measure the complex refractive index and determine

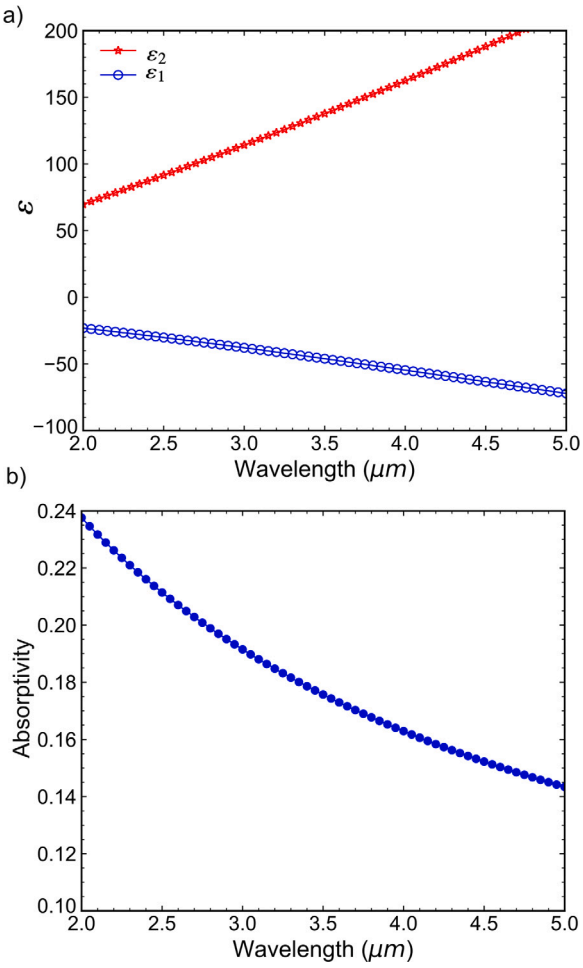

Fig. 5. (a) Real (ε_1) and imaginary (ε_2) components of the dielectric function for the 316L-AM-HD in the spectral range of the IR camera measured via IR-VASE. (b) absorption as a function of wavelength across the camera's detection band.

the complex dielectric function over the wavelength range of the IR camera ($\varepsilon_1, \varepsilon_2$), as described in Eq. (1). The complex dielectric function was measured at different angles and at different sample rotations to take into account surface heterogeneity. The complex dielectric function for sample 316L-AM-HD is shown in Fig. 5a, these values were then used to calculate the spectral emissivity via the Fresnel equations, Eq. (2). Finally, the total emissivity over the wavelength range of the IR camera (from 2.0 μm to 5 μm), Fig. 5b, was determined using Planck's law. The ratio of the integration of the spectral radiance of the sample to that of a blackbody gives the total (normal) emissivity over the wavelength range of the camera. For 316L-AM-M and 316L-AM-HD, the spectral emissivity is 0.18 ± 0.002, which aligns with literature [42,43], and for 316L-AM-LD the spectral emissivity is 0.21 ± 0.01.

$$\tilde{n} - ik = \sqrt{\tilde{\varepsilon}} = \sqrt{\varepsilon_1 + i\varepsilon_2}, \tag{1}$$

$$\epsilon_\lambda = 1 - R(\lambda) = 1 - \left[\frac{\tilde{n}(\lambda) - 1}{\tilde{n}(\lambda) + 1}\right]^2. \tag{2}$$

Once the true temperature as a function of radius is determined, a mathematical model was employed to fit the radial temperature distribution under steady-state conditions. This model determines a temperature differential (ΔT) that can be used to calculate the thermal conductivity (κ) by fitting the model to the experimental data. The predicted temperature differential induced from the laser heating is based on the heat equation in cylindrical coordinates:

$$\frac{\partial^2 T}{\partial r^2}(r,z,t) + \frac{1}{r}\frac{\partial T}{\partial r}(r,z,t) + \frac{\partial^2 T}{\partial z^2}(r,z,t) + \frac{S}{\kappa}(r,z,t) = \frac{1}{\alpha}\frac{\partial T}{\partial t}. \tag{3}$$

Here, S is the total heat flux as a function of r, z, and t, κ is the thermal conductivity, and α denotes the thermal diffusivity. When considering only temperature under steady-state conditions ($\partial T/\partial t = 0$), Eq. (3) simplifies to:

$$\frac{1}{r}\frac{d}{dr}\left(r\frac{dT}{dr}\right) + \left(\frac{d^2T}{dz^2}\right) = -\frac{Q(r)}{\kappa}, \tag{4}$$

where Q represents the heat source generated by a laser with a Gaussian profile, expressed as:

$$Q(r) = \frac{2p}{\pi r_o^2} exp\left(-\frac{2r^2}{r_o^2}\right). \tag{5}$$

In Eq. (5), p denotes the incident laser power in Watts, and r_o represents the $1/e^2$ laser radius. Because sample dimensions are much larger than both the laser spot size and the radial distance over which the temperature profile is analyzed, the problem is consider semi-infinite and we impose an insulated boundary condition at the radial edge ($r = R$) and specify a heat flux boundary condition at the surface $z = 0$ to solve Eq. (4). These are expressed as:

$$\left.\frac{\partial T}{\partial r}\right|_{r=R} = 0, \quad \left. -\kappa\frac{\partial T}{\partial z}\right|_{z=0} = Q(r). \tag{6}$$

This formalism is readily solved with zero-order Hankel transform for temperature and heat flux, given by:

$$\overline{T}(\lambda, z) = \int_0^\infty T(r,z) J_0(\lambda r) r dr, \tag{7a}$$

$$\overline{Q}(\lambda) = \int_0^\infty Q(r,z) J_0(\lambda r) r dr. \tag{7b}$$

The Hankel Transformation for the terms on the left side of Eq. (4) is:

$$H_0\left[\frac{1}{r}\frac{\partial}{\partial r}\left(r\frac{\partial T}{\partial r}\right)\right] = \int_0^\infty r J_0(\lambda r)\left[\frac{1}{r}\frac{\partial}{\partial r}\left(r\frac{\partial T}{\partial r}\right)\right] dr = -\lambda^2\overline{T}, \tag{8a}$$

$$H_0\left[\frac{\partial T}{\partial z}\right] = \int_0^\infty r J_0(\lambda r)\left[\frac{\partial T}{\partial z}\right] dr = \frac{\partial \overline{T}}{\partial z}. \tag{8b}$$

With identities Eqs. (8a) and (8b), we rewrite Eq. (4) and use an insulated boundary condition at $z = 0$ to obtain an ordinary differential equation:

$$\frac{\partial \overline{T}}{\partial z} - \lambda^2\overline{T} = 0. \tag{9}$$

After solving Eq. (9), the inverse Hankel transform at $z = 0$ of this problem yields:

$$\Delta T(r,0) = \frac{1}{k}\int_0^\infty \overline{Q}(\lambda) J_0(\lambda r) d\lambda. \tag{10}$$

This integral is evaluated numerically using the Python SciPy library.

An example of SSLITHER data showing a change in temperature as a function of radial distance and corresponding model fits on 316L-M and 316L-AM-HD samples is shown in Fig. 6. Our measured value for the thermal conductivity of 316L-M of 14.9 ± 0.4 W m^{-1} K^{-1} agrees well with literature values: 14.3 ± 0.16 W m^{-1} K^{-1} [44] and 14.3 ± 1.4 W m^{-1} K^{-1} [45]. The SSLITHER data on the 316L-AM-HD sample exhibits a larger temperature rise as compared to the 316L-M sample, consistent with a lower thermal conductivity, which we determine from our model fit to these data as 13.0 ± 0.5 W m^{-1} K^{-1}, approximately 20% lower than the machined sample. We attribute the small perturbation in temperature decay of the 316L-AM-HD around 0.6 mm away from the center of the laser spot to surface porosity observed in Fig. 2b. We discuss the origin of the observed thermal conductivity changes in the AM samples in Section 4.

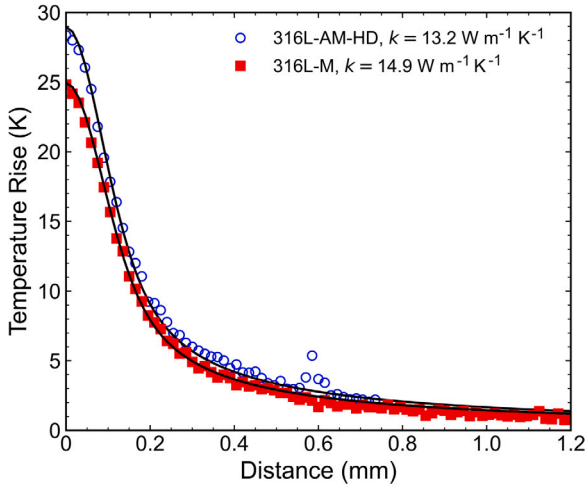

Fig. 6. Thermal conductivity of 316L-M and effective thermal conductivity of 316L-AM-HD at 0.55 W output power measured via SSLITHER. The difference in ΔT is driven by a decrease in thermal conductivity of approximately 20%. Squares and dots represent raw data from the machined and AM sample, respectively, while the solid line corresponds to the mathematical model fit.

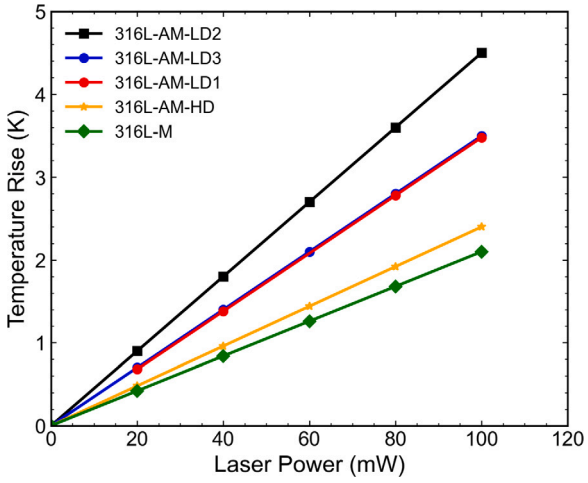

Fig. 7. Steady state temperature rise as a function of incident laser power for all samples measured via TOPS. The machined sample exhibits the highest thermal conductivity (and thus lowest temperature rise), while 316L-AM-LD1, 316L-AM-LD2, and 316L-AM-LD3 show the lowest effective thermal conductivities (highest temperature rises) due to high porosity.

3.2. Thermal conductivity measurements with TOPS

To validate and support our thermal conductivity measurements with SSLITHER, we also measure the thermal conductivity of the samples with a Thermo-Optical Plane Source (TOPS) technique (Laser Thermal's TOPS instrument). An in-depth description of the operating principle and analysis of TOPS is discussed elsewhere [40]. In short, like SSLITHER, TOPS measures the temperature change of a laser-heated surface of a sample during steady-state conditions. In our particular TOPS measurements, we use a 1 mm $1/e^2$ diameter laser spot. However, unlike SSLITHER, in which we heat and probe the surface of the sample directly, thus requiring knowledge of the sample absorptivity at the laser wavelength and total emissivity of the sample within the spectral bandwidth of the IR camera, TOPS utilizes a thin black tape transducer applied to the laser-heated surface of the sample. The emissivity/absorptivity of the black tape at the IR camera and laser wavelengths are known, and thus the absorbed laser power and temperature rise of the sample are known *a priori*. The temperature rise in the center of the laser-heated region is monitored as a function of laser power to determine the thermal conductivity (unlike SSLITHER, which monitors the temperature change as a function of radius in and away from the laser-heated volume). Using the solution to the steady-state heat equation at $r = 0$, which corresponds to the center of the Gaussian laser beam, where the temperature rise is maximum. With this the thermal conductivity is then determined [40,46,47].

An example of TOPS data of change in temperature vs. change in laser power on all samples studied in this work is shown in Fig. 7. We can qualitatively conclude trends from these data, as a higher ΔT or a given change in laser power immediately translates to a lower thermal conductivity. Consistent with our SSLITHER data, the AM samples have a lower effective thermal conductivity than the machined sample, and the lower density AM samples have lower thermal conductivities than the higher density AM sample. We discuss these trends and present all measured results in Section 4.

3.3. Melting temperature and high temperature emissivity measurements

We measure the melting temperature (solidus and liquidus temperatures) of our samples using the high power laser setup shown in Fig. 8, consisting of a 4.0 kW Yb:YAG continuous-wave laser ($\lambda = 1.03$ μm), a 256-channel spectropyrometer (FMP2-2X) from 500 nm to 1000 nm and a single color pyrometer (Impac IS 140) at 676 nm. The spectropyrometer has a spot size of 2 mm in diameter, which is large enough to represent an area to average effective emissivity over a region containing local surface heterogeneity, additionally, the spectropyrometer wavelength range provides sensitive to small temperature differences. The sample is supported by two zirconia disks in a chamber that is first evacuated to 1.0×10^{-5} bar, and then backfilled with argon to purge residual oxygen. Additionally, an electrochemical oxygen pump is used to deplete oxygen to a partial pressure of 2×10^{-20} atm. We then heat the surface of the sample with our kW laser, using a 7.5 mm-diameter beam with a tophat beam profile to ensure a uniform temperature distribution across the laser-heated surface. The change of temperature is recorded using the single color pyrometer positioned at the center of the laser spot with a field of view of 1.5 mm. The single color pyrometer measures the radiance temperature, T_{rad}, at 676 nm. To obtain the true temperature, T, the radiance temperature was corrected using Wien's law, Eq. (11), and the emissivity obtained from the multi wavelength spectropyrometer at the same wavelength. The determination of spectral emissivity with spectropyrometry is described in detail elsewhere [48].

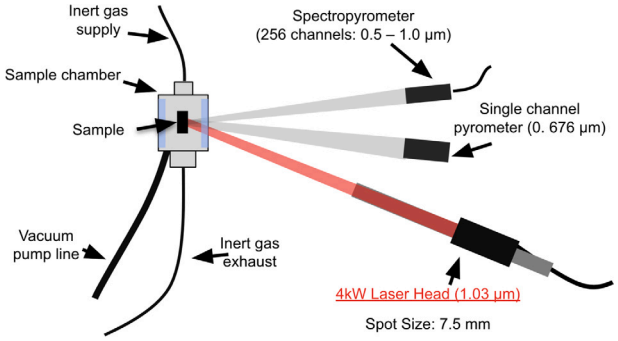

Fig. 8. High power laser setup used to measure solidus and liquidus temperatures.

$$\frac{1}{T} = \frac{1}{T_{rad}} + \frac{\lambda}{C_2} \ln\left(\epsilon(\lambda, T)\right), \tag{11}$$

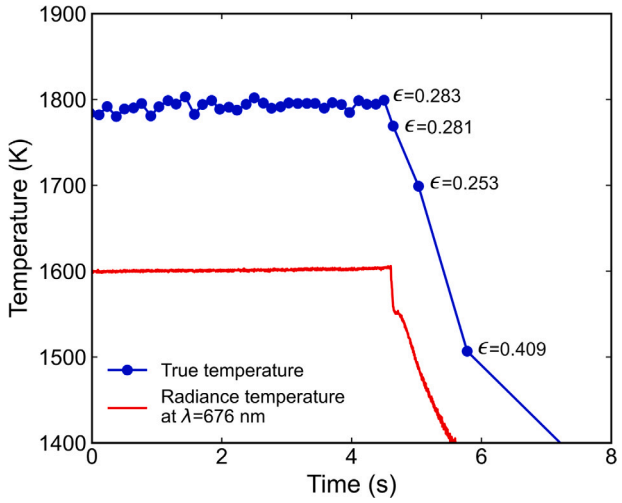

Fig. 9. High density sample (316L-AM-HD) radiance temperature measured via the single color pyrometer is lower than true temperature (extracted from the spectropyrometer). The resolidification plateau is observed in the radiance temperature change of the single color pyrometer, and is emissivity corrected to true temperature using the emissivity measured via the spectropyrometer at the same point in time during resolidification ($\epsilon = 0.25 \pm 0.04$).

Table 2
Comparison of effective thermal conductivity obtained using the SSLITHER method and the Laser Thermal TOPS system.

Sample	SSLITHER k [W m^{-1} K^{-1}]	TOPS k [W m^{-1} K^{-1}]
316L-M	14.9 ± 0.4	14.0 ± 0.7
316L-AM-HD	13.0 ± 0.5	13.9 ± 0.6
316L-AM-LD1	9.4 ± 0.5	9.8 ± 0.5
316L-AM-LD2	6.5 ± 0.6	7.1 ± 0.3
316L-AM-LD3	9.8 ± 0.8	9.7 ± 0.5
316L-AM-LD3 (post melt)	13.0 ± 0.5	

where C_2 is the second radiation constant and $\epsilon(\lambda, T)$ is the emissivity at wavelength λ.

As expected, T_{rad} monitored from the single color pyrometer is lower than the true temperature T, which is determined from the emissivity correction employed by the spectropyrometer. This is exemplified in Fig. 9, which shows the measured temperatures and converted to true temperature of sample 316L-AM-HD as a function of time during conditions when the laser is heating the sample to induce a molten pool in the laser-heated volume, then the laser is turned off, allowing the laser-heated volume to cool. The key in employing both of these pyrometric measurements, in addition to determining $\epsilon(\lambda, T)$, is that the spectropyrometer operates with a variable time step, with a minimum interval of approximately 40 ms, compared to the single color pyrometer's 1 ms temporal resolution. As determination of the resolidification dynamics during cooling requires the observation of thermal arrests in the temperature vs. time thermographs [49], the time scale of this recalescence can often occur over temporal windows faster than the spectropyrometer time constants. Thus, the spectropyrometer is used to determine emissivity around the resolidification plateaus that is then used to emissivity-correct the radiance temperature measured by the single color pyrometer, the latter of which has the temporal resolution to resolve the recalescence associated with resolidification. While the emissivity can certainly change from molten to partially molten or solid states during cooling and resolidification, we find that the emissivity of our samples remains relatively constant across these transitions. For example, the emissivity of 316L-AM-HD varies by ±0.02 during resolidification, until it reaches its fully solid state, when emissivity changes drastically as illustrated in Fig. 9. This stability allows us to adopt this emissivity value, along with its upper and lower bounds, to determine the liquidus and solidus temperatures, discussed in the following section.

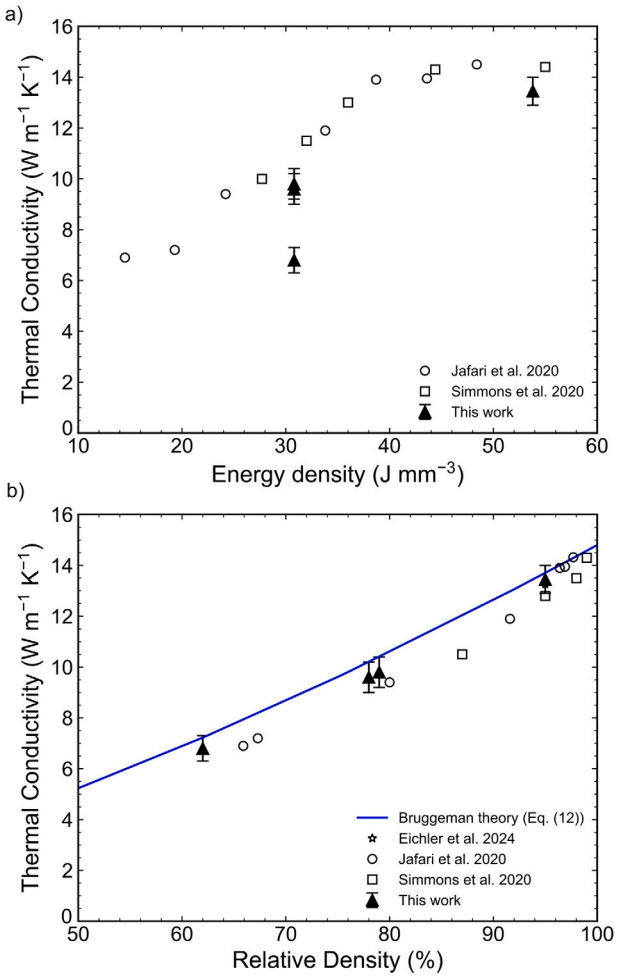

Fig. 10. Effective thermal conductivity (κ) of additively manufactured 316L stainless steel as a function of (a) volumetric energy density and (b) relative density. In both cases, the effective thermal conductivity increases with higher energy input and densification. Data from this work are compared with literature values from Simmons et al. [24], Jafari et al. [50], and Eichler et al. [51]. Error bars represent the uncertainty arising from variations in laser spot size, absorbed power, and repeatability. More details about uncertainty are provided in the supplementary material, Section S1.

4. Results and discussion

The measured thermal conductivities of all the samples studied in this work are tabulated in Table 2. Given the highly porous nature of the low density samples observed in our SEM micrographs, this effective thermal conductivity reduction is not surprising as an increased porosity is well known to reduce κ due to reductions in density [52]. Interestingly, one of the low density AM samples, 316L-AM-LD2, exhibited a lower effective thermal conductivity than the 316L-AM-LD1 and 316L-AM-LD3 samples, despite being printed under identical conditions. This is illustrated in Fig. 10a, which plots the measured effective thermal conductivity vs. energy density during printing ($E_d = P/vht$, Table 1).

When the energy density during printing is lower than 40 J mm^{-3}, the relative density of the final AM part can drop substantially [3]. Thus, at these low energy densities, we cannot ensure that each low

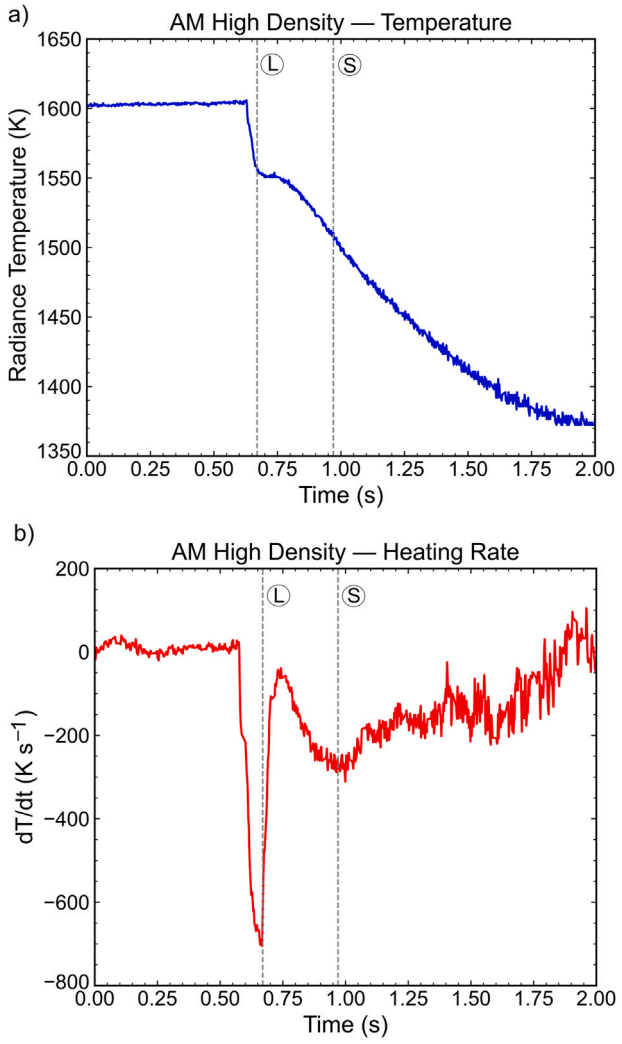

Fig. 11. A comparison of the radiance temperature during resolidification of the 316L-AM-HD sample (a), and the first derivative of this temperature over time (b). The temperature derivative shows the peaks where temperature experiences a variation due to phase changes allowing for the determination of liquidus (L) and solidus (S) temperature.

density AM sample has the same relative density. Thus, we use the Archimedes method to measure the density of our samples, which we show in Fig. 10b by plotting measured effective thermal conductivity as a function of relative density. Our data exhibit a monotonic trend between effective thermal conductivity and relative density, a trend expected from effective medium theories for thermal conductivity of porous media. For example, we show calculations for thermal conductivity reductions as a function of relative density via the unsymmetric Bruggeman theory [53] that relates porosity, ϕ, to the reduced thermal conductivity via:

$$\kappa_{\text{porous}} = (1-\phi)^{1.5}\kappa_{\text{fully dense}}, \tag{12}$$

which agrees well with the trend in both our data and additional data on AM 316L from the literature.

The reduced densities of the 316L-AM-LD samples as compared to the machined and 316L-AM-HD samples should also manifest in reduced high temperature performance, which we study here in relation to the samples' resolidification dynamics around the melting point. Specifically, from the resolidification thermograms tracking temperature as a function of time when the sample is cooling from melt

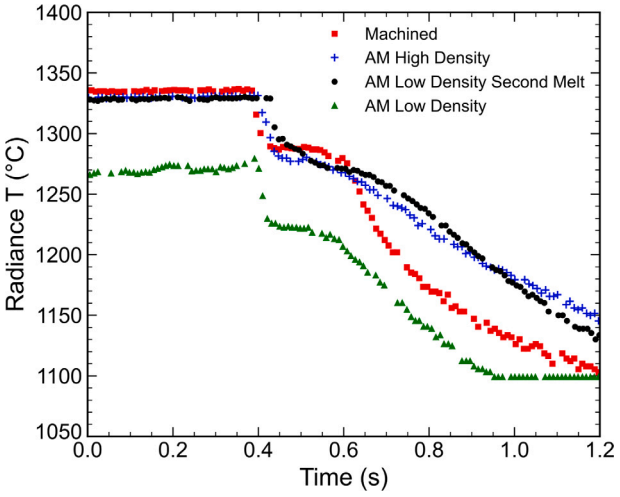

Fig. 12. Time-resolved radiance temperature during laser melting of machined, AM high-density, and AM low-density 316L samples. The AM low-density (green triangles) exhibits a lower radiance temperature and apparent melting point, consistent with the presence of LOF and porosity. At the second melt at the same location (black circles), the low-density sample shows an increased radiance temperature comparable to the dense conditions, indicating recovery of the melting behavior. (For interpretation of the references to color in this figure legend, the reader is referred to the web version of this article.)

(Fig. 11a). We compute the first derivative of temperature with respect to time ($\partial T/\partial t$), which enables identification of subtle non-monotonic changes in the cooling profile associated with phase transformations [54]. When solidification begins, the release of latent heat causes a deviation from the smooth cooling trend, which appears as a distinct change in the derivative. The start of nucleation is marked by a visible drop in $\partial T/\partial t$ [55], typically corresponding to the liquidus temperature (Fig. 11b), and corresponds to complete melting of the alloy during laser exposure. As cooling progresses, the derivative reaches a local minimum at the solidus temperature, marking the completion of solidification (Fig. 11(a and b), dotted horizontal line, marked 's'). The solidus temperature marks the temperature below which the alloy is completely solidified (above this temperature and below the liquidus the alloy is partially molten). The temperature interval between solidus and liquidus plays a crucial role in pore evolution, affecting porosity, cracking susceptibility, and inter-layer bonding [56]. Thus, evaluation of solidus and liquidus temperatures of the AM samples as compared to machined samples provides an evaluation of high temperature performance of these parts.

The experimentally measured solidus and liquidus temperatures for 316L-M, 316L-AM-HD and 316L-AM-LD3 are summarized in Table 3. Our measured solidus and liquidus temperatures on the 316L-M sample align well with values reported in the literature [57], validating the accuracy of our approach.

In the low-density AM sample, we observed a significantly narrower melting range: the liquidus temperature 1679 ± 15 K, and the solidus was 1598 ± 15 K, a difference of about 35 K compared to the machined and high density AM sample (Fig. 12). We attribute this difference in non-equilibrium solidus and liquidus to lack of fusion areas (LOF), as observed in Fig. 2c. These LOF regions are not just voids but complex features that carry oxides and dislocation structures [18,19,58]. These oxides can affect the melting behavior and shift the temperatures away from equilibrium, Yang et al. [59] reported that the full melting temperature can deviate from theoretical values, and this shift depends on the oxide concentration. They further showed that these oxides significantly affect the solidification of the SS-316L and deviate from the equilibrium cooling [60].

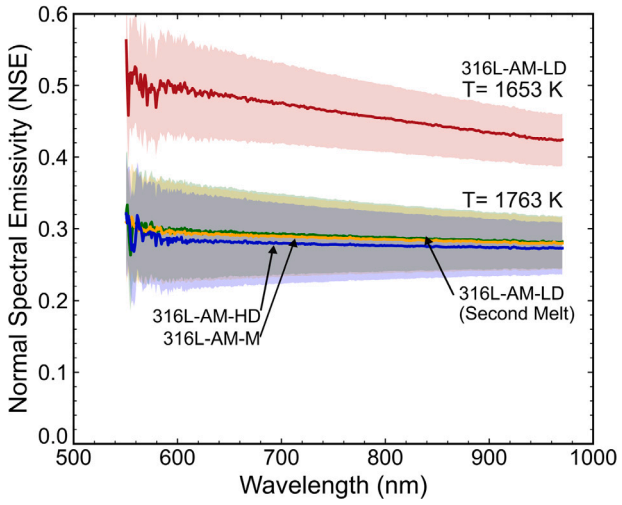

Fig. 13. Normal spectral emissivity (NSE) as a function of wavelength for high density sample (316L-AM-HD) and low density (316L-AM-LD). During the first melt the low-density sample shows elevated emissivity at 1653 K across the measured spectral range, attributed to lack-of-fusion (LOF) defects. After remelting at the same location, the emissivity of the low-density sample decreases to match that of the high-density material. Additionally, it could reach a temperature comparable to that of the machined and high density sample (1763 K), indicating densification and removal of LOF defects. 2σ uncertainties reported, description of how uncertainties were calculated is found in the supplementary material, Section 2.

Additionally, these oxides increase the emissivity of the material [61]. It has been observed that emissivity generally increases as the oxygen enriched region becomes thicker, primarily due to interference effects arising from multiple reflections between the metal substrate and the growing oxide region [62]. Consistent with this, we measured an increase in the normal spectral emissivity (from the cooling curve) to approximately 0.5 during the first melt (Fig. 13). We attribute this enhanced emissivity to transient surface oxidation and/or the presence of LOF [63].

To understand the origin and evolution of these oxides, we focus on how oxygen is redistributed during melting and solidification. It has been shown that during solidification, oxygen, initially present in the melt and at the surface, moves toward the edge of the melt pool as a consequence of surface-active solutes modifying the surface tension, causing oxygen to migrate outward during melting [63]. This behavior is evident in Fig. 14, where Energy-Dispersive Spectroscopy (EDS) shows oxygen enrichment at the edge of the laser melting spot while in the laser spot oxygen is not present.

When the same location is remelted, the normal spectral emissivity decreases to approximately 0.3 (Fig. 13), and we observe a recovery of the non-equilibrium solidus and liquidus temperatures on 316L-AM-LD3 that is comparable with those of the 316L-M and 316L-AM-HD samples (Table 3, Fig. 12). We interpret this recovery as a consequence of repeated melting, which disrupts or partially removes the oxygen-enriched, oxide-rich features and reduces the effective oxide thickness [62], thereby restoring emissivity and melting behavior closer to those of the fully dense material [63].

Additionally, the effective thermal conductivity of 316L-AM-LD3 after this second melting test increased to a value comparable to that of 316L-AM-HD (Table 2), aligning with our finding that reduced density of the AM samples directly impacts the effective thermal conductivity of AM parts. However, emissivity and the measured solidus/liquidus temperatures are strongly influenced by local surface condition, oxygen enrichment, and the thermal history of the melted region. Therefore, lower relative density is an indicator of more surface defects, which increases the probability of local oxygen regions that cause heterogeneous melting behavior, rather than as a single parameter that uniquely affects emissivity or phase transition temperatures. Consistent with this interpretation, the low-density AM sample shows the largest reduction in effective thermal conductivity and the largest deviation in emissivity and melting behavior, while remelting partially restores the measured properties toward those of the high-density and machined samples. This emphasizes the potential for laser-based thermal conductivity, emissivity and melting temperature measurements as a means to evaluate the properties of AM materials and performance.

Table 3
Liquidus and solidus true temperatures for machined and additively manufactured (AM) samples. Uncertainties come from calibration of the spectropyrometer and single color pyrometer, deviation of determined emissivity, repeatability of measurements and first derivative approach to select solidus and liquidus temperature points.

Sample	Liquidus (K)	Solidus (K)
316L-M	1718 ± 13	1650 ± 10
316L-AM-HD	1714 ± 13	1637 ± 9
316L-AM-LD3	1679 ± 15	1598 ± 15
316L-AM-LD3 (post melt)	1729 ± 15	1625 ± 15

5. Conclusion

In this work we combined two steady-state, non-contact thermography techniques, SSLITHER and the commercial tool from Laser Thermal TOPS, to quantify how additive manufacturing process parameters and resulting defects alter the thermal behavior of 316L stainless steel. Additionally, we measure emissivity and non-equilibrium liquidus and solidus using a non-contact method with a high power laser. In summary, this study shows that:

- The thermal conductivity measurements using SSLITHER were consistent with those obtained from TOPS, validating the accuracy of our non-contact measurement method. Additionally, SSLITHER offered the precision and resolution required to capture local defects in AM parts.
- High density AM shows 20% lower effective thermal conductivity than machined, while low density AM (316L-AM-LD3) shows a 50% reduction in effective thermal conductivity. This trend follows the energy density-relative density expectations explained in Fig. 10.
- High-temperature experiments revealed that porosity and the presence of lack of fusion (LOF) structure in the low density sample significantly impact the liquidus and solidus temperatures, showing a narrower melting interval.
- Normal spectral emissivity is strongly influenced by surface condition: low-density regions and LOF defects lead to higher emissivity, whereas after remelting the emissivity returns to values comparable to the denser sample 316-AM-HD.
- EDS analysis reveals that oxygen is localized at the rim of the laser spot, confirming that LOF regions play a key role in the modified emissivity and melting characteristics.
- Effective thermal conductivity is recovered, with numbers similar to the 316-AM-HD sample after melting, where the melted region is denser and free from LOF.

These results show that steady-state laser-based thermography can diagnose changes in thermal conductivity, emissivity, and melting behavior caused by printing parameters associated with surface defects. These experiments highlight the critical role of accurate thermal characterization in understanding melting behavior and phase transitions.

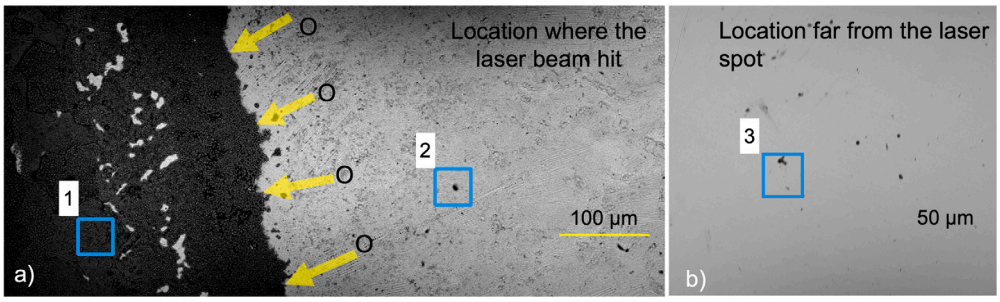

Fig. 14. SEM micrographs and EDS analysis of the low-density 316L-AM-LD3 sample. (a) Region at the edge of the laser spot, where oxygen is enriched at the outer rim: point 1 (rim) contains 9.79 wt% oxygen, while point 2 (inside the laser spot) shows no detectable oxygen. (b) Region far from the laser spot, where point 3 also shows no detectable oxygen, indicating that oxygen is localized at the outer rim of the laser-irradiated area. Elemental compositions are provided in Tables S1-S3 (Supplementary Material).

CRediT authorship contribution statement

Jessica Reyes: Writing – original draft, Visualization, Investigation, Formal analysis, Conceptualization. **Hunter B. Schonfeld:** Writing – review & editing, Methodology, Investigation. **Jeffrey L. Braun:** Validation, Resources, Data curation. **Saman Zare:** Writing – review & editing, Methodology, Investigation. **Bryan N. Baines:** Validation, Resources, Data curation. **John T. Gaskins:** Validation, Resources. **Michael A. Gallegos:** Resources. **David Saiz:** Resources. **Bryan Kaehr:** Resources. **Patrick E. Hopkins:** Writing – review & editing, Supervision, Resources, Project administration, Methodology, Funding acquisition, Conceptualization.

Declaration of competing interest

The authors declare the following financial interests/personal relationships which may be considered as potential competing interests: Patrick E. Hopkins, Jeffrey L. Braun, Bryan N. Baines and John T. Gaskins reports financial support and statistical analysis were provided by Laser Thermal. Patrick E. Hopkins, Jeffrey L. Braun, Bryan N. Baines and John T. Gaskins reports a relationship with Laser Thermal that includes: employment and non-financial support. If there are other authors, they declare that they have no known competing financial interests or personal relationships that could have appeared to influence the work reported in this paper.

Acknowledgments

We appreciate support from the Office of Naval Research, United States, Grant No. N00014-26-1-2076 and The Advanced Research Projects Agency-Energy (ARPAE), U.S. Department of Energy, United States, under Award Number DE-AR0001998. This work was performed, in part, at the Center for Integrated Nanotechnologies, an Office of Science User Facility operated for the U.S. Department of Energy (DOE) Office of Science. Sandia National Laboratories is a multimission laboratory managed and operated by National Technology & Engineering Solutions of Sandia, LLC, a wholly owned subsidiary of Honeywell International, Inc., for the U.S. DOE's National Nuclear Security Administration under contract DE-NA-0003525. The views expressed in the article do not necessarily represent the views of the U.S. DOE or the United States Government.

Appendix A. Supplementary data

Supplementary material related to this article can be found online at https://doi.org/10.1016/j.ijheatmasstransfer.2026.129055.

Data availability

Data will be made available on request.

References

[1] B. Blakey-Milner, P. Gradl, G. Snedden, M. Brooks, J. Pitot, E. Lopez, M. Leary, F. Berto, A. du Plessis, Metal additive manufacturing in aerospace: A review, Mater. Des. 209 (2021) 110008, http://dx.doi.org/10.1016/j.matdes.2021.110008.

[2] B. Zhang, L. Dembinski, C. Coddet, The study of the laser parameters and environment variables effect on mechanical properties of high compact parts elaborated by selective laser melting 316L powder, Mater. Sci. Eng.: A 584 (2013) 21–31, http://dx.doi.org/10.1016/j.msea.2013.06.055.

[3] M. Zhang, C.-N. Sun, X. Zhang, P.C. Goh, J. Wei, D. Hardacre, H. Li, Fatigue and fracture behaviour of laser powder bed fusion stainless steel 316L: Influence of processing parameters, Mater. Sci. Eng.: A 703 (2017) 251–261, http://dx.doi.org/10.1016/j.msea.2017.07.071.

[4] S. Siddique, M. Imran, M. Rauer, M. Kaloudis, E. Wycisk, C. Emmelmann, F. Walther, Computed tomography for characterization of fatigue performance of selective laser melted parts, Mater. Des. 83 (2015) 661–669, http://dx.doi.org/10.1016/j.matdes.2015.06.063.

[5] M. Akita, Y. Uematsu, T. Kakiuchi, M. Nakajima, R. Kawaguchi, Defect-dominated fatigue behavior in type 630 stainless steel fabricated by selective laser melting, Mater. Sci. Eng.: A 666 (2016) 19–26, http://dx.doi.org/10.1016/j.msea.2016.04.042.

[6] R. Shrestha, J. Simsiriwong, N. Shamsaei, S.M. Thompson, L. Bian, Effect of build orientation on the fatigue behavior of stainless steel 316l manufactured via a laser-powder bed fusion process, in: Solid Freeform Fabrication 2016: Proceedings of the 27th Annual International Solid Freeform Fabrication Symposium – an Additive Manufacturing Conference, University of Texas at Austin, Austin, TX, 2016, pp. 605–616.

[7] L. Zhang, D. Klemm, J. Eckert, Y. Hao, T. Sercombe, Manufacture by selective laser melting and mechanical behavior of a biomedical Ti–24Nb–4Zr–8Sn alloy, Scr. Mater. 65 (1) (2011) 21–24, http://dx.doi.org/10.1016/j.scriptamat.2011.03.024.

[8] D. Saltzman, M. Bichnevicius, S. Lynch, T.W. Simpson, E.W. Reutzel, C. Dickman, R. Martukanitz, Design and evaluation of an additively manufactured aircraft heat exchanger, Appl. Therm. Eng. 138 (2018) 254–263, http://dx.doi.org/10.1016/j.applthermaleng.2018.04.032.

[9] R. Carter, S. Draper, I. Locci, B. Lerch, D. Ellis, P. Senick, M. Meyer, J. Free, K. Cooper, Z. Jones, Materials characterization of additively manufactured components for rocket propulsion, in: International Astronautical Congress, Vol. GRC-E-DAA-TN26762, 2015.

[10] A.T. Nelson, Prospects for additive manufacturing of nuclear fuel forms, Prog. Nucl. Energy 155 (2023) 104493, http://dx.doi.org/10.1016/j.pnucene.2022.104493.

[11] G. Chen, Nanoscale Energy Transport and Conversion: A Parallel Treatment of Electrons, Molecules, Phonons, and Photons, in: MIT-Pappalardo Series in Mechanical Engineering, Oxford University Press, Oxford ; New York, 2005.

[12] M.R. Islam, P. Karna, J.A. Tomko, E.R. Hoglund, D.M. Hirt, M.S.B. Hoque, S. Zare, K. Aryana, T.W. Pfeifer, C. Jezewski, A. Giri, C.D. Landon, S.W. King, P.E. Hopkins, Evaluating size effects on the thermal conductivity and electron–phonon scattering rates of copper thin films for experimental validation of Matthiessen's rule, Nat. Commun. 15 (9167) (2024) 1–9, http://dx.doi.org/10.1038/s41467-024-53441-9, Open Access.

[13] E.A. Scott, K. Hattar, C.M. Rost, J.T. Gaskins, M. Fazli, C. Ganski, C. Li, T. Bai, Y. Wang, K. Esfarjani, M. Goorsky, P.E. Hopkins, Phonon scattering effects from point and extended defects on thermal conductivity studied via ion irradiation of crystals with self-impurities, Phys. Rev. Mater. 2 (9) (2018) 095001, http://dx.doi.org/10.1103/PhysRevMaterials.2.095001.

[14] G. Chen, Nanoscale heat conduction in solids, in: Nanoscale Energy Transport and Conversion: A Parallel Treatment of Electrons, Molecules, Phonons, and Photons, in: MIT-Pappalardo Series in Mechanical Engineering, Oxford University Press, Oxford ; New York, 2005, pp. 25–70, (Chapter 2).

[15] C. Kamath, B. El-dasher, G.F. Gallegos, W.E. King, A. Sisto, Density of additively-manufactured, 316L SS parts using laser powder-bed fusion at powers up to 400 W, Int. J. Adv. Manuf. Technol. 74 (1–4) (2014) 65–78, http://dx.doi.org/10.1007/s00170-014-5954-9.

[16] C. Ye, C. Zhang, J. Zhao, Y. Dong, Effects of Post-processing on the Surface Finish, Porosity, Residual Stresses, and Fatigue Performance of Additive Manufactured Metals: A Review, J. Mater. Eng. Perform. 30 (9) (2021) 6407–6425, http://dx.doi.org/10.1007/s11665-021-06021-7.

[17] S.A. Khairallah, A.T. Anderson, A. Rubenchik, W.E. King, Laser powder-bed fusion additive manufacturing: Physics of complex melt flow and formation mechanisms of pores, spatter, and denudation zones, Acta Mater. 108 (2016) 36–45, http://dx.doi.org/10.1016/j.actamat.2016.02.014.

[18] P. Deng, M. Karadge, R.B. Rebak, V.K. Gupta, B.C. Prorok, X. Lou, The origin and formation of oxygen inclusions in austenitic stainless steels manufactured by laser powder bed fusion, Addit. Manuf. 35 (2020) 101334, http://dx.doi.org/10.1016/j.addma.2020.101334.

[19] M. Laleh, A.E. Hughes, S. Yang, J. Wang, J. Li, A.M. Glenn, W. Xu, M.Y. Tan, A critical insight into lack-of-fusion pore structures in additively manufactured stainless steel, Addit. Manuf. 38 (2021) 101762, http://dx.doi.org/10.1016/j.addma.2020.101762.

[20] D.-W. Oh, J. Ravichandran, C.-W. Liang, W. Siemons, B. Jalan, C.M. Brooks, M. Huijben, D.G. Schlom, S. Stemmer, L.W. Martin, A. Majumdar, R. Ramesh, D.G. Cahill, Thermal conductivity as a metric for the crystalline quality of SrTiO3 epitaxial layers, Appl. Phys. Lett. 98 (22) (2011) 221904, http://dx.doi.org/10.1063/1.3579993.

[21] K.E. Meyer, R. Cheaito, E. Paisley, C.T. Shelton, J.L. Braun, J.-P. Maria, J.F. Ihlefeld, P.E. Hopkins, Crystalline coherence length effects on the thermal conductivity of MgO thin films, J. Mater. Sci. 51 (23) (2016) 10408–10417, http://dx.doi.org/10.1007/s10853-016-0261-5.

[22] E.A. Scott, K. Hattar, J.L. Braun, C.M. Rost, J.T. Gaskins, T. Bai, Y. Wang, C. Ganski, M. Goorsky, P.E. Hopkins, Orders of magnitude reduction in the thermal conductivity of polycrystalline diamond through carbon, nitrogen, and oxygen ion implantation, Carbon 157 (2020) 97–105, http://dx.doi.org/10.1016/j.carbon.2019.09.076.

[23] B.F. Donovan, D.M. Long, A. Moballegh, N. Creange, E.C. Dickey, P.E. Hopkins, Impact of intrinsic point defect concentration on thermal transport in titanium dioxide, Acta Mater. 127 (2017) 491–497, http://dx.doi.org/10.1016/j.actamat.2017.01.018.

[24] J.C. Simmons, X. Chen, A. Azizi, M.A. Daeumer, P.Y. Zavalij, G. Zhou, S.N. Schiffres, Influence of processing and microstructure on the local and bulk thermal conductivity of selective laser melted 316L stainless steel, Addit. Manuf. 32 (2020) 100996, http://dx.doi.org/10.1016/j.addma.2019.100996.

[25] K. Bartsch, B. Bossen, W. Chaudhary, M. Landry, D. Herzog, Thermal conductivity of Ti-6Al-4V in laser powder bed fusion, Front. Mech. Eng. 8 (2022) 830104, http://dx.doi.org/10.3389/fmech.2022.830104.

[26] L.C. Wei, L.E. Ehrlich, M.J. Powell-Palm, C. Montgomery, J. Beuth, J.A. Malen, Thermal conductivity of metal powders for powder bed additive manufacturing, Addit. Manuf. 21 (2018) 201–208, http://dx.doi.org/10.1016/j.addma.2018.02.002.

[27] A. Abou-Sena, A. Ying, M. Abdou, Experimental measurements of the effective thermal conductivity of a lithium titanate (Li2TiO3) pebbles-packed bed, J. Mater. Process. Technol. 181 (2007) 206–212, http://dx.doi.org/10.1016/j.jmatprotec.2006.03.061.

[28] Standard test method for evaluating the resistance to thermal transmission by the guarded heat flow meter technique, 2019, http://dx.doi.org/10.1520/E1530-19, Current edition approved Feb. 1, 2019. Originally approved 1993; last previous edition 2016.

[29] P. Zhang, Y. Xuan, Q. Li, Effect of surface roughness on thermal contact resistance of aluminium alloy, Appl. Therm. Eng. 121 (2017) 992–998, http://dx.doi.org/10.1016/j.applthermaleng.2017.04.142.

[30] D.G. Cahill, et al., Analysis of heat flow in layered structures for time-domain thermoreflectance, Rev. Sci. Instrum. 75 (12) (2004) 5119.

[31] A.J. Schmidt, R. Cheaito, M. Chiesa, A frequency-domain thermoreflectance method for the characterization of thermal properties, Rev. Sci. Instrum. 80 (9) (2009).

[32] J.L. Braun, D.H. Olson, J.T. Gaskins, P.E. Hopkins, A steady-state thermoreflectance method to measure thermal conductivity, Rev. Sci. Instrum. 90 (2) (2019).

[33] I. Minervini, P. Yang, H. Higgins, E. Ziade, Thermal Conductivity of AM Fabricated Stainless Steel 316L Part, Tech. Rep. SAND–2023-00335, 2432179, 2023, http://dx.doi.org/10.2172/2432179.

[34] Y.V.M.X.L. Jamison, L. Bartlett, F.M. Heim, In situ defect detection in selective laser melting via full-field infrared thermography, Addit. Manuf. 24 (2018) 595–605, http://dx.doi.org/10.1016/j.addma.2018.10.045.

[35] S. Moylan, E. Whitenton, B. Lane, J. Slotwinski, Infrared thermography for laser-based powder bed fusion additive manufacturing processes, AIP Conf. Proc. 1581 (2014) 1191–1196, http://dx.doi.org/10.1063/1.4864956.

[36] K.C.S. Price, K. Cooper, Evaluations of temperature measurements by near-infrared thermography in Powder-Based Electron-Beam additive manufacturing, University of Texas at Austin, 2012, pp. 761–773.

[37] M. Reza Yavari, R.J. Williams, K.D. Cole, P.A. Hooper, P. Rao, Thermal modeling in metal additive manufacturing using graph theory: Experimental validation with laser powder bed fusion using in situ infrared thermography data, J. Manuf. Sci. Eng. 142 (12) (2020) 121005, http://dx.doi.org/10.1115/1.4047619.

[38] B.S. Kai Zeng, A review of thermal analysis methods in laser sintering and selective laser melting, in: Proceedings of the Solid Freeform Fabrication Symposium, University of Texas at Austin, 2012, pp. 796–814.

[39] M. Milich, H.B. Schonfeld, K. Boboridis, D. Robba, L. Vlahovic, R.J.M. Konings, J.L. Braun, J.T. Gaskins, N. Bhatt, A. Giri, P.E. Hopkins, Validation of the Wiedemann-Franz law in solid and molten Tungsten above 2000 K through thermal conductivity measurements via steady-state temperature differential radiometry, Phys. Rev. Lett. 132 (2024) 146303, http://dx.doi.org/10.1103/PhysRevLett.132.146303.

[40] J.L. Braun, B.N. Baines, J.T. Gaskins, P.E. Hopkins, A thermo-optical plane source method to measure thermal conductivity, Rev. Sci. Instrum. 96 (7) (2025) 074901, http://dx.doi.org/10.1063/5.0267492.

[41] https://www.infratec-infrared.com/thermography/wegweiser/physical-principles/.

[42] D. Dewitt, Thermophysical properties of matter-the TPRC data series. Volume 7. Thermal radiative properties-metallic elements and alloys, 1970.

[43] J.L. King, H. Jo, A. Shahsafi, K. Blomstrand, K. Sridharan, M.A. Kats, Impact of corrosion on the emissivity of advanced reactor structural alloys, J. Nucl. Mater. 508 (2018) 465–471.

[44] T.W. Watson, H.E. Robinson, Thermal Conductivity of a Sample of Type 316 Stainless Steel, Tech. Rep. NBS Report 7818, National Bureau of Standards, Washington, D.C., 1963, Report to Applied Physics Laboratory, Johns Hopkins University, Silver Spring, Maryland.

[45] K.C. Mills, Recommended Values of Thermophysical Properties for Selected Commercial Alloys, first ed., Woodhead Publishing, Cambridge, 2002, http://dx.doi.org/10.1533/9781845690144.

[46] J.L. Braun, D.H. Olson, J.T. Gaskins, P.E. Hopkins, A steady-state thermoreflectance method to measure thermal conductivity, Rev. Sci. Instrum. 90 (2) (2019) 024905, http://dx.doi.org/10.1063/1.5056182.

[47] J.L. Braun, P.E. Hopkins, Upper limit to the thermal penetration depth during modulated heating of multilayer thin films with pulsed and continuous wave lasers: A numerical study, J. Appl. Phys. 121 (17) (2017).

[48] R.A. Felice, The spectropyrometer – a practical multi-wavelength pyrometer, in: Proceedings of the 8th Symposium on Temperature: Its Measurement and Control in Science and Industry, FAR Associates, Macedonia, OH, 2002, Presented October 21–24, 2002.

[49] D. Manara, M. Sheindlin, W. Heinz, C. Ronchi, New techniques for high-temperature melting measurements in volatile refractory materials via laser surface heating, Rev. Sci. Instrum. 79 (11) (2008) 113901.

[50] D. Jafari, W.W. Wits, T.H. Vaneker, A.G. Demir, B. Previtali, B.J. Geurts, I. Gibson, Pulsed mode selective laser melting of porous structures: Structural and thermophysical characterization, Addit. Manuf. (2020) http://dx.doi.org/10.1016/j.addma.2020.101263, Journal Pre-proof version.

[51] F. Eichler, N. Balc, S. Bremen, P. Nink, Investigation of laser powder bed fusion parameters with respect to their influence on the thermal conductivity of 316L samples, J. Manuf. Mater. Process. 8 (4) (2024) 166, http://dx.doi.org/10.3390/jmmp8040166.

[52] R.M. Costescu, A.J. Bullen, G. Matamis, K.E. O'Hara, D.G. Cahill, Thermal conductivity and sound velocities of hydrogen-silsesquioxane low-k dielectrics, Phys. Rev. B 65 (9) (2002) 094205, http://dx.doi.org/10.1103/PhysRevB.65.094205.

[53] D.A.G. Bruggeman, Berechnung verschiedener physikalischer konstanten von heterogenen substanzen. I. Dielektrizitätskonstanten und leitfähigkeiten der mischkörper aus isotropen substanzen, Ann. Phys., Lpz. 416 (7) (1935) 636–664, http://dx.doi.org/10.1002/andp.19354160705.

[54] O. Fornaro, H.A. Palacio, Study of dilute Al–Cu solidification by cooling curve analysis, J. Mater. Sci. 44 (16) (2009) 4342–4347, http://dx.doi.org/10.1007/s10853-009-3648-8.

[55] A.I. Savvatimskiy, S.V. Onufriev, G.V. Valyano, A.A. Nepapushev, D.O. Moskovskikh, Thermophysical properties of tantalum carbide (TaC) within 2000–5500 K temperature range, Ceram. Int. 48 (14) (2022) 19655–19661, http://dx.doi.org/10.1016/j.ceramint.2022.03.102.

[56] K. Zhang, Y. Chen, S. Marussi, X. Fan, M. Fitzpatrick, S. Bhagavath, M. Majkut, B. Lukic, K. Jakata, A. Rack, M.A. Jones, J. Shinjo, C. Panwisawas, C.L.A. Leung, P.D. Lee, Pore evolution mechanisms during directed energy deposition additive manufacturing, Nat. Commun. 15 (1) (2024) 1715, http://dx.doi.org/10.1038/s41467-024-45913-9.

[57] P. Pichler, B.J. Simonds, J.W. Sowards, G. Pottlacher, Measurements of thermophysical properties of solid and liquid NIST SRM 316l stainless steel, J. Mater. Sci. 55 (2020) 4081–4093, http://dx.doi.org/10.1007/s10853-019-04261-6.

[58] X. He, R.I. Revilla, D. Kong, X. Ni, W. Zhang, K. Dai, C. Dong, The nature of oxide films in process-induced lack-of-fusion defects on laser powder bed fusion-fabricated hastelloy X Ni-based alloy, Addit. Manuf. 101 (2025) 104709, http://dx.doi.org/10.1016/j.addma.2025.104709.

[59] X. Yang, F. Gao, F. Tang, X. Hao, Z. Li, Effect of surface oxides on the melting and solidification of 316L stainless steel powder for additive manufacturing, Met. Mater. Trans. A 52 (10) (2021) 4518–4532, http://dx.doi.org/10.1007/s11661-021-06405-3.

[60] X. Yang, F. Tang, X. Hao, Z. Li, Oxide evolution during the solidification of 316l stainless steel from additive manufacturing powders with different oxygen contents, Met. Mater. Trans. B 52 (4) (2021) 2253–2262, http://dx.doi.org/10.1007/s11663-021-02191-w.

[61] G. Mohr, S. Nowakowski, S.J. Altenburg, C. Maierhofer, K. Hilgenberg, Experimental determination of the emissivity of powder layers and bulk material in laser powder bed fusion using infrared thermography and thermocouples, Metals 10 (11) (2020) 1546, http://dx.doi.org/10.3390/met10111546.

[62] T. Iuchi, T. Furukawa, S. Wada, Emissivity modeling of metals during the growth of oxide film and comparison of the model with experimental results, Appl. Opt. 42 (13) (2003) 2317–2326.

[63] H.Y. Chia, L. Wang, W. Yan, Influence of oxygen content on melt pool dynamics in metal additive manufacturing: High-fidelity modeling with experimental validation, Acta Mater. 249 (2023) 118824, http://dx.doi.org/10.1016/j.actamat.2023.118824.